

## Strategy for Synthesizing Porous Cellulose Nanocrystal Supported Metal Nanocatalysts

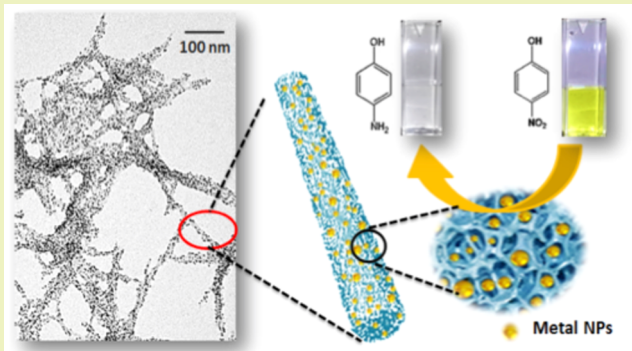
Xinyun Wu,<sup>†</sup> Zengqian Shi,<sup>†</sup> Sidong Fu,<sup>†</sup> Jialu Chen,<sup>†</sup> Richard M Berry,<sup>‡</sup> and Kam C. Tam\*,<sup>†</sup>

<sup>†</sup>Department of Chemical Engineering, Waterloo Institute for Nanotechnology, University of Waterloo, Waterloo, Ontario, Canada, N2L3G1

<sup>‡</sup>CelluForce Inc., 625, Président-Kennedy Avenue, Montreal, Quebec, Canada H3A 1K2

### Supporting Information

**ABSTRACT:** This paper describes a novel platform to prepare small and uniformly distributed metal nanoparticles (MNPs) on cellulose nanocrystals for use as high performance sustainable nanocatalysts. The model platinum or palladium NPs (1–2 nm in size) were immobilized and chemically reduced onto melamine-formaldehyde (MF) coated cellulose nanocrystals (MFCNCs). The MF coating was critical for the uniform generation and size-control of MNPs. The contribution of MF resin to optimal MNP synthesis includes: (1) increased surface area with its spongelike structure, (2) enhanced affinity to metals through chelation with nitrogen functionalities, and (3) effective MNP size control due to the mesoporous structure. The MNP/MFCNC system significantly improved catalytic activity as demonstrated by the reduction of 4-nitrophenol with Pd/MFCNCs with a turnover frequency of  $3168\text{ h}^{-1}$ . Our synthesis does not require any complicated apparatus or harsh reaction conditions. The proposed strategy is well-suited for the synthesis of a wide range of metal nanocatalysts characterized by a particle size of 1 to 2 nm and superior catalytic activity.



**KEYWORDS:** Cellulose nanocrystals, Platinum, Melamine formaldehyde, Supported catalyst, 4-Nitrophenol

### INTRODUCTION

Metal nanocatalysis is a developing field of research where metal nanoparticles (MNPs) offer dramatically increased surface area, chemical activity, specificity of interaction, and unprecedented efficiency compared to their bulk counterparts.<sup>1</sup> However, the preparation of MNPs is challenging due to the tendency of NPs to minimize surface energy by aggregation resulting in a loss of catalytic activity. The recyclability of MNPs can also be challenging and it affects both the economics and environmental footprint. One promising strategy to address the stability and reusability is to immobilize MNPs on a suitable substrate. A wide range of solid supports including mesoporous silica,<sup>2,3</sup> metal–organic frameworks,<sup>4,5</sup> carbon-based materials,<sup>6,7</sup> etc. have been evaluated. In recent years, research activity on the use of biomass-derivatives as the supporting substrates has intensified since they are widely available, inexpensive, nontoxic, ecofriendly, and biodegradable. Many metal nanoparticles have been successfully immobilized onto biomass-derived materials such as cellulose,<sup>8</sup> chitosan,<sup>9</sup> starch,<sup>10,11</sup> etc. As catalytic supports, some biomaterials also have the advantages of high sorption capacity, affinity with metal ions, as well as physical and chemical versatility that allow easy surface functionalization and structural engineering into different forms including flakes, gel beads, membranes, fibers,

hollow fibers, and sponge.<sup>12</sup> One such biomaterial is cellulose nanocrystal (CNC).

CNCs are the crystalline domains extracted from wood fiber through acid hydrolysis, and they are excellent substrates for anchoring MNPs. CNC possesses the attractive features of a well-controlled rod structure with high surface area, high stability in water, and superior mechanical properties unmatched by other forms of cellulose derivatives.<sup>13,14</sup> CelluForce, a Canadian company, is operating the world's first demonstration plant that uses a continuous process capable of producing 1000 kg of CNCs per day. Using CNCs to support MNPs is an emerging new field. Monodispersed Pd nanoparticles on CNCs have been produced by reducing  $\text{PdCl}_2$  with  $\text{H}_2$ .<sup>15</sup> The prepared Pd/CNC better catalyzed hydrogenation and Heck-coupling reactions than PdNPs loaded on  $\text{Al}_2\text{O}_3$  or carbon supports. Other metals, such as AuNPs,<sup>16–19</sup> AgNP,<sup>20</sup> and PtNPs<sup>21,22</sup> have also been successfully immobilized on CNCs. However, the field of heterogeneous catalysis

**Special Issue:** Building on 25 Years of Green Chemistry and Engineering for a Sustainable Future

**Received:** March 21, 2016

**Revised:** June 24, 2016

**Published:** July 29, 2016

by MNPs supported by CNC is still in its infancy. Some of the opportunities on the synthesis of MNPs/CNC hybrids are the use of nontoxic reducing agents in benign conditions,<sup>23</sup> better size control of MNPs,<sup>23,24</sup> and the effective functionalization of CNCs to enhance the affinity with NMPs.<sup>25</sup> One challenge is that CNCs have an impermeable surface<sup>13</sup> whereas porous surfaces have proven to offer extra benefits of increased accessible sites for particle adsorption, inhibition of particle growth, and reduction of particle aggregation.<sup>26,27</sup>

In this paper, we report on the synthesis of a core–shell structured melamine-formaldehyde (MF) coated CNC as a novel mesoporous substrate to support MNP catalysts. Two types of metal Pt and Pd were selected for the deposition on MFCNC to illustrate the versatility of the proposed approach. Notably, uniform 1 to 2 nm Pd and Pt NPs were synthesized and immobilized on MFCNC. The critical role of the surface modification of CNC with MF resin becomes apparent when compared to the significantly poorer MNP deposition on pristine CNCs. The multiple contributions of mesoporous MF resin are (1) increased surface area due to the sponge-like porous matrix, (2) the chelation of MNPs and enhanced metal ion affinity through the rich nitrogen functionalities of the MF resin,<sup>28,29</sup> and (3) the confined growth of MNPs in the mesopores of MF resin. To validate the catalytic activity of the synthesized MFCNC supported metal nanocatalysts, Pd/MFCNC was selected for the model catalytic reduction of 4-nitrophenol by NaBH<sub>4</sub>. The hybrid nanocatalyst demonstrated superior catalytic activity with a very high turnover frequency (TOF) of 3168 h<sup>-1</sup>. The strategy of using porous MF/CNC as the template for MNP synthesis could be applied to various metals and extended to metal oxides to achieve ultrafine particle size with greatly improved catalytic performance.

## EXPERIMENTAL SECTION

**Materials.** CNCs were provided by Celluforce Inc. and were produced by sulfuric acid hydrolysis of pulp, purified, and then spray dried. CNCs produced using this approach are readily redispersed under sonication to yield a stable suspension due to negatively charged sulfate ester groups on the CNC surface. All the chemicals used in this study were analytical grade, purchased from Sigma-Aldrich, and used as received.

**Synthesis of MFCNCs.** In a typical synthesis, 2.2 g of melamine and 4.0 mL of formaldehyde (37% in water) was mixed in 10 mL deionized water in a 50 mL flask under magnetic stirring. The pH of the mixture was then adjusted to between 8 and 9 using NaOH solution and the reaction temperature was elevated to 80 °C. After 30 min, the precursor of MF was formed and 100 mL of 0.5% CNC suspension was introduced, the pH was adjusted with 1 M HCl solution to around 4. The suspension was stirred overnight at 80 °C. During the process, the cross-linked MF resin condenses on the CNC surface to yield a coating. The suspension was then allowed to cool to room temperature and purified by repeated ultrafiltration.

**Synthesis of Metal-MFCNCs.** A 10 mg portion of MFCNC was dispersed in 20 mL of ethylene glycol that acts as a dispersant and a reducing agent. Then 20 mg of chloroplatinic acid hexahydrate (37.5% metal basis) or 10 mg potassium tetrachloropalladate was added to the above solution and the pH was adjusted to 8.0 using 1 M NaOH. Then the mixture was refluxed at 110 °C for 2 h followed by repeated filtration. Pd/Pt-CNC were prepared using the same conditions with pristine CNCs.

**Characterization.** The morphology of CNC was characterized using a JEM-2100 high resolution TEM (HRTEM). The CNC sample was stained with 2% (w/w) uranyl acetate negative stain for high resolution imaging. The morphology of MFCNC, Pt/MFCNC, Pd/MFCNC, Pt/CNC, and Pd/CNC were characterized using a Philips CM10 transmission electron microscope (TEM). The surface charges

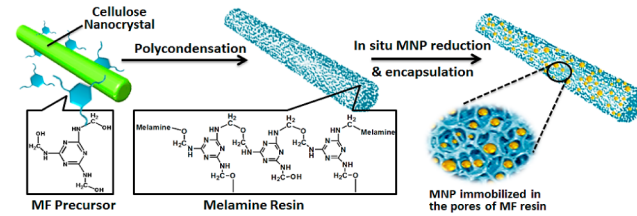
of the MFCNC and CNC were measured using a Malvern Zetasizer Nano ZS (Worcestershire, UK) where the zeta potential of the particles was calculated from the electrophoretic mobility values using the Smoluchowski equation. The sample particles were well dispersed in Millipore water at neutral pH before the zeta potential measurements. The coating of MF on CNC was further confirmed and characterized by FT-IR (PerkinElmer 1720 FT-IR spectrometer). For the FT-IR spectrum, freeze-dried samples were mixed with KBr and then compressed into pellets for measurements at a resolution of 4 cm<sup>-1</sup>. The thermal stability of the synthesized MFCNC was determined from thermal gravimetric analysis (TGA) where the samples were placed in an inert ceramic crucible and heated from 25 to 800 °C at a heating rate of 10 °C min<sup>-1</sup> under a flow of N<sub>2</sub> at 20 mL min<sup>-1</sup>. Samples are completely dried in the vacuum oven overnight at 60 °C to eliminate the influences of water prior to the TGA test. The loading of Pt and Pd NPs in the hybrid material of Pt/MFCNC and Pd/MFCNC was also determined from TGA where samples were heated from 25 to 800 °C at a heating rate of 10 °C min<sup>-1</sup> in air atmosphere at 10 mL min<sup>-1</sup>. X-ray diffraction (XRD) was performed with the Rigaku D/MAX-RB diffractometer using filtered Cu K $\alpha$  radiation for all samples prepared. The surface area of the samples was determined by N<sub>2</sub> adsorption analysis with an autosorb iQ-AG instrument (Quantachrome Co., USA) at 77° K using the multipoint BET (Brunauer–Emmett–Teller) model and the pore size distribution curves, pore volume and pore diameter were obtained from the analysis of N<sub>2</sub> adsorption isotherms using Barrett–Joyner–Halenda (BJH) method using the Kelvin model of pore filling. Prior to measurements, the samples were degassed overnight at 150 °C under vacuum.

**Catalytic Performance Test.** The catalytic activity of Pd/MFCNC was tested by the reduction of 4-nitrophenol (4-NP) to 4-aminophenol (4-AP) using NaBH<sub>4</sub> as the reducing agent. In a typical test, 4-NP (0.16 mM) was first mixed with fresh NaBH<sub>4</sub> (0.032 M) aqueous solution (the molar ratio of NaBH<sub>4</sub> to 4-NP was 200:1) from which 1 mL of the mixture solution was transferred to a UV-vis cuvette. A 10 μL portion of Pd/MFCNC (0.025 mg/mL) was pipetted into the cuvette followed by rapid mixing with the pipet over 2 s. The kinetics of the reaction at room temperature was monitored every minute by UV-vis scans between 250 and 600 nm. Apparent kinetic constants were obtained from the decay of UV-vis spectra of the reactant by assuming that the reaction is pseudo-first order.

## RESULTS AND DISCUSSION

**Scheme 1** outlines our strategy for preparing the supported porous MFCNC and MNP hybrid system. It consists of two

**Scheme 1. Schematic of the Preparation of MNP/MFCNC**



steps: (1) the functionalization of CNC with MF resin to form the core–shell MFCNC structure and (2) the reduction of MNPs onto the MFCNC. In the first step, well-dispersed CNC particles in aqueous suspension allow their high surface area to be fully accessible to the MF prepolymer which is anchored and grows from the surface of CNCs. The introduction of MF resin is key to adding surface porosity and nitrogen functional groups to support MNP deposition. In the second step, metal precursors were introduced in the presence of ethylene glycol as a weak reducing agent. The porous MF resin provides an environment where metal ions are readily reduced to metals

and confined to the pores of MF resin. Further stabilization is also offered through the nitrogen–metal interaction due to amine functionalities of MF resin.

The morphologies of CNC and MFCNC were characterized by TEM. Figure 1a shows the high resolution TEM image of

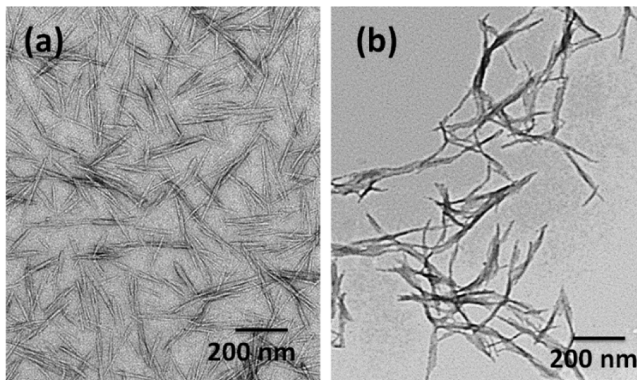


**Figure 1.** (a) High resolution TEM for pristine CNCs with uranyl acetate staining and (b) TEM image for MFCNC.

CNC, where the typical rod-shaped CNC particles with a diameter around 5 nm and 150–200 nm in length was observed. It should be noted that CNC needs to be stained in order to yield a better image (i.e., higher contrast) under TEM. After the surface modification, the CNCs became slightly thicker in diameter, and appears much darker without staining (Figure 1b), confirming the successful coating of MF resin on the CNCs. The coating of MF resin not only preserves the structural features of CNCs, but it also introduces critical advantages of MF resin including high porosity and nitrogen functionalities that are beneficial for further metal immobilization.

To further confirm the presence of MF in the MFCNC system, FTIR characterization was performed on both pristine CNCs and MFCNCs and the results are shown in Figure 2a. Several new peaks were evident in the MFCNCs spectrum that were absent in the pristine CNC system: a peak at  $1552\text{ cm}^{-1}$  due to N–H bending of the bridging secondary amine; a peak at  $812\text{ cm}^{-1}$  due to bending vibration of the 3, 5-triazine ring, and a peak at  $1330\text{ cm}^{-1}$  due to the methylene C–H bending vibration of melamine.<sup>30,31</sup> Further evidence was provided by zeta potential (ZP) measurements. Pristine CNCs possessed a zeta-potential of  $-54\text{ mV}$  due to the negatively charged sulfate ester groups on the surface, whereas the ZP of MFCNCs increased to  $+40\text{ mV}$ . These results suggest a complete coverage of CNCs with MF resin. The composition of the synthesized MFCNC was estimated from thermal gravimetric analysis (TGA). From the TGA results shown in Figure 2b, the thermodegradation curves showed that the residue at  $600\text{ }^{\circ}\text{C}$  was 19.8% for CNC, 29.8% for MFCNC, and 42.4% for pure MF resin. From this information, the MF resin content in MFCNC was calculated to be 44.2% based on the following equations:

$$C_{\text{CNC}} + C_{\text{MF}} = 1 \quad (1)$$

$$0.198C_{\text{CNC}} + 0.424C_{\text{MF}} = 0.298 \quad (2)$$

where  $C_{\text{CNC}}$  and  $C_{\text{MF}}$  is the mass ratio of CNC and MF in MFCNC, respectively. A higher degradation rate at lower temperature region was observed for MFCNC compared to

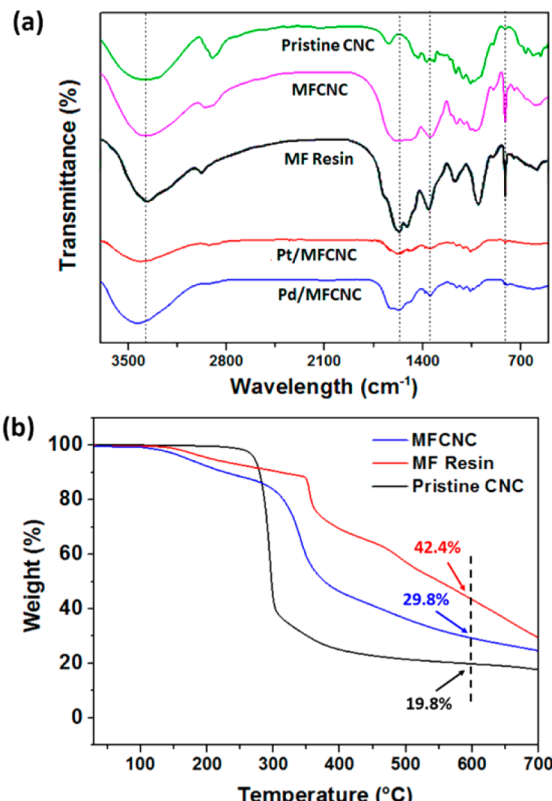


**Figure 2.** (a) FTIR characterization for CNC, MFCNC, MF resin, Pt-MFCNC, and Pd-MFCNC and (b) TGA measurements for MF resin, MFCNC, and CNC under  $\text{N}_2$ .

MF resin. This is mainly due to the size and surface area effects related to the finer-structured MF coating on CNCs compared to its bulk counterpart. Similar phenomena have also been observed for melamine/urea-formaldehyde resin and  $\text{LiCoO}_2$ .<sup>32,33</sup>

The detailed structural change for CNCs before and after MF coating was analyzed by BET analysis. The  $\text{N}_2$  adsorption/desorption isotherm is presented in Figure 3 where the volume of adsorbate ( $\text{N}_2$ ) adsorbed on the surface of adsorbent (MFCNC) at standard temperature and pressure (STP) were plotted against relative pressure of  $P/P_0$  (the pressure at equilibrium over saturation pressure of adsorbates) at a

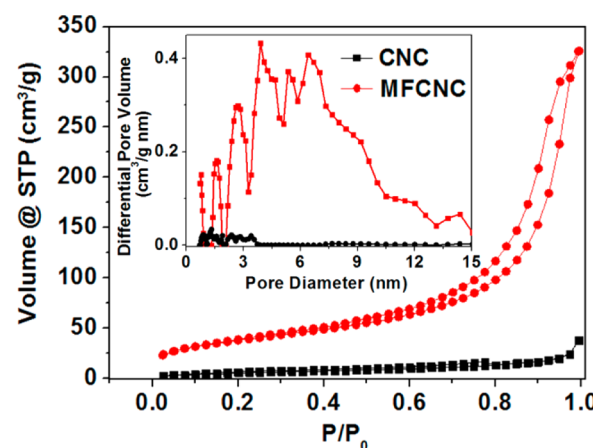


**Figure 3.**  $\text{N}_2$  adsorption/desorption isotherms of CNCs and MFCNCs. (inset) Corresponding PSDs of both samples.

constant temperature. Pristine CNCs possessed a multi-BET surface area of  $24.12 \text{ m}^2 \text{ g}^{-1}$  with a rather poor pore structure. The lower surface area of CNCs measured compared to their calculated theoretical value is due to the formation of packed lamellar structure during drying which have been observed in many studies.<sup>34–36</sup> As mentioned earlier, the surface of CNCs is smooth and nonporous. This is confirmed by the BET results that show a typical nonporous type II isotherm<sup>37</sup> with an extremely low pore volume of  $0.001 \text{ cm}^3 \text{ g}^{-1}$ . However, when CNCs were coated with a layer of MF resin, the hybrid material displayed a type IV isotherm<sup>38</sup> associated with a mesoporous structure. The pore size distribution (PSD) curve expressing pore volume fraction as a function of pore diameter is shown in the inset of Figure 3. Intense peaks shown over a wide range of the mesopore region strongly suggest the essence of abundant mesopores in the MFCNC structure. Moreover, multi-BET surface area for MFCNCs was determined to be  $212.8 \text{ m}^2 \text{ g}^{-1}$  with a pore volume of  $0.071 \text{ cm}^3 \text{ g}^{-1}$  and a mean pore diameter of  $1.34 \text{ nm}$ . It should also be noted that the higher surface area obtained in MFCNCs could be attributed to both the mesoporous structure of MF resin as well as the suppression of packing of CNCs. However, the mesopores within  $2\text{--}15 \text{ nm}$  range shown in PSD curve can only be generated by the MF resin.

The well-controlled Pt and Pd deposition supported by MFCNCs is confirmed by TEM imaging (Figure 4a and c).

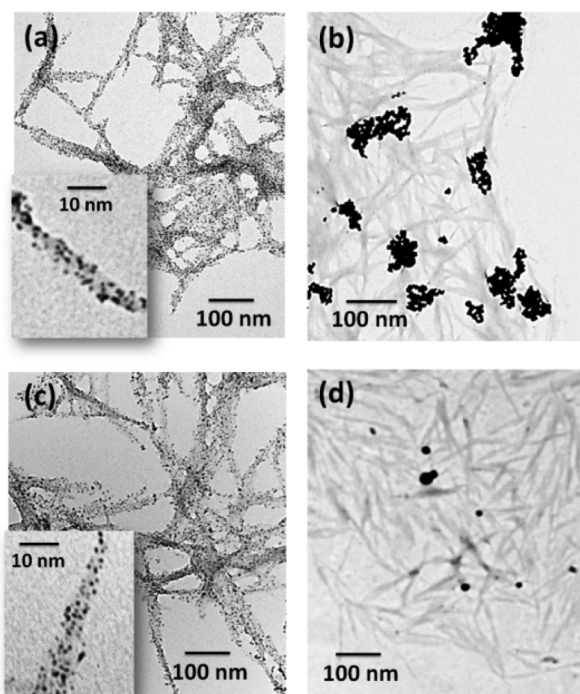


**Figure 4.** TEM images of (a) Pt-MFCNC, (b) Pt-CNC, (c) Pd-MFCNC, and (d) Pd-CNC.

The homogeneous reduction of MNPs was achieved; and monodispersed Pt and Pd particles of  $1\text{--}2 \text{ nm}$  in size were anchored and uniformly distributed on the surface of MFCNCs with negligible agglomeration. The critical role of functionalizing CNCs with MF resin was further validated by performing the same metal reduction in the presence of unmodified CNCs. As shown in Figure 4b and d, Pt MNPs were agglomerated and nonuniformly distributed on the surface of the CNCs, while Pd

MNPs were barely reduced. In both cases, pristine CNCs without the MF shell were not suitable substrates for metal deposition.

Pt/MFCNCs and Pd/MFCNCs were also characterized by FT-IR (Figure 2a) to investigate the interaction between MNPs and MF resin. When compared to the MFCNC spectrum, there is no new peak in either the Pt-MFCNC or Pd-MFCNC spectrum indicating that no chemical bond was formed between the MF resin and MNPs. However, the sharp peak at  $812 \text{ cm}^{-1}$  caused by 3,5-triazine ring bending was dramatically reduced after metal deposition. The broad band at  $3500\text{--}3300 \text{ cm}^{-1}$  due to the superposition of O–H and N–H stretching of the MF resin<sup>39</sup> slightly shifted to a higher wavenumber. These changes could potentially be associated with the chelating effect of nitrogen atoms on the MF resin with Pd and Pt.

Figure 5a shows the X-ray diffraction patterns of CNCs, MFCNCs, Pt/MFCNCs, and Pd/MFCNCs, respectively. Peaks

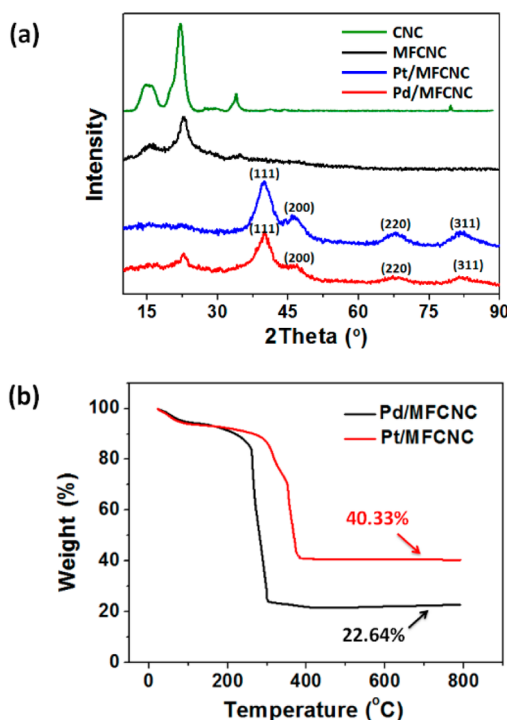


**Figure 5.** (a) XRD pattern of the pristine CNCs, MFCNCs, Pt/MFCNCs, and Pd/MFCNCs. (b) TGA analysis with an air atmosphere to determine the metal content in Pt/MFCNCs and Pd/MFCNCs.

in the MFCNC and CNC patterns at  $2\theta = 14.9^\circ$ ,  $16.2^\circ$ ,  $22.6^\circ$ , and  $34.4^\circ$ , correspond to the  $(\bar{1}10)$ ,  $(110)$ ,  $(200)$ , and  $(004)$  crystallographic planes, respectively.<sup>40</sup> The patterns for Pt/MFCNCs and Pd/MFCNCs displayed several sharp new peaks at  $2\theta$  around  $39.6^\circ$ ,  $46.2^\circ$ ,  $67.5^\circ$ , and  $81.4^\circ$ . These are associated with the characteristic  $(\bar{1}11)$ ,  $(200)$ ,  $(220)$ , and  $(311)$  crystalline planes of metal Pt and Pd, possessing face-centered-cubic (fcc) structures.<sup>41,42</sup> XRD results confirmed that the crystal structures of these MNPs are not affected by the MFCNC substrate. For both samples, the diffraction spectra are very broad, indicating small nanoparticles.

The average crystal size of Pt and Pd can be calculated from Pt(111) reflections with the Scherrer equation:<sup>43</sup>

$$D_p = \frac{0.9\lambda}{\beta \cos \theta} \quad (3)$$

where  $D_p$  is the average crystal size,  $\lambda$  is X-ray wavelength (0.154 Å),  $\beta$  is the full width at half-maximum (fwhm) of the peak in radians,  $\theta$  is the Bragg angle. The Pt and Pd cluster sizes calculated for Pt/MFCNC and Pd/MFCNC catalysts were 1.86 and 1.78 nm, respectively. These results are very close to the results determined by TEM analysis. The exact Pt and Pd loading in the hybrid system of MNP/MFCNCs were determined by TGA shown in Figure 5b. The TGA test was conducted under air atmosphere where all organic components in the composites were completely decomposed in the presence of oxygen, leaving the MNPs as the residue. The residue was determined to be 40.33% for Pt in Pt/MFCNCs and 22.64% for Pd in Pd/MFCNCs. The stability of MNPs on the substrate was verified by exposing the material in harsh sonication treatment for 30 min. TEM images taken for the sonicated composite material in water shows that the MNPs are still well stabilized on the substrate without delaminating to the bulk solution. Therefore, the leaching of MNPs in our system is negligible. (Figure S1).

In order to demonstrate the catalytic activity of our porous MFCNC supported MNP system, the catalytic reduction of 4-NP was performed using NaBH<sub>4</sub> catalyzed by Pd/MFCNCs. The reduction of *p*-nitrophenol is considered an ideal model reaction to evaluate the catalytic activity of various metallic nanoparticle systems,<sup>44</sup> and it is also of importance in wastewater treatment due to their anthropogenic, toxic, and inhibitory nature of *p*-nitrophenol.<sup>45</sup> Figure 6a shows the time-dependent UV-vis adsorption spectra for the reduction of 4-NP catalyzed by Pd/MFCNC. The conversion of 4-NP to 4-AP was complete within 13 min in the presence of Pd/MFCNC, as

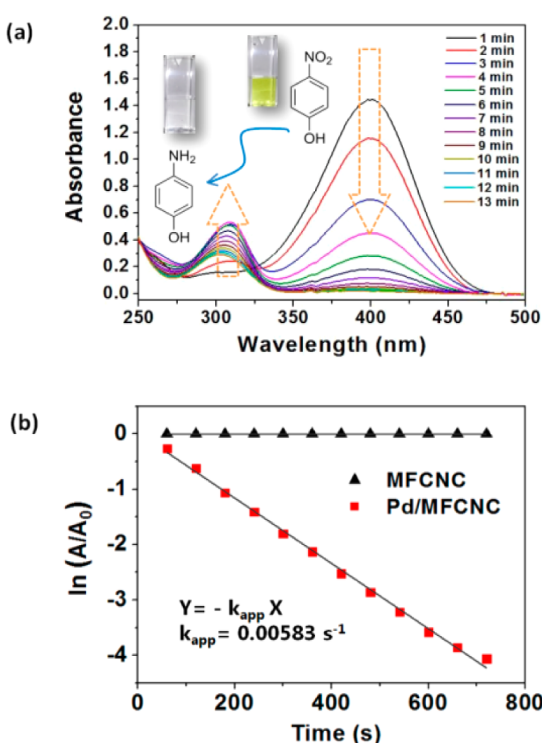


**Figure 6.** (a) Time-dependent UV-vis spectra of the 4-nitrophenol reduction catalyzed by Pd/MFCNCs and (b)  $\ln(A/A_0)$  versus reaction time  $t$  at 400 nm.

revealed by the diminished adsorption peak at 400 nm, together with the appearance of a new peak at 310 nm. The completion of the reaction is accompanied by a change in the color of the solution from yellow to colorless. In contrast, no reduction was found when only MFCNCs was tested, indicating that Pd NPs are responsible for catalyzing the reduction of 4-NP to 4-AP.

Since the reduction of 4-NP proceeds in the presence of an excess of NaBH<sub>4</sub>, the reaction is generally considered pseudo-first-order and independent of the borohydride content. To correlate our results to the model,  $\ln(A_t/A_0)$  was plotted against time in Figure 6b, where the absorbance was obtained from the absorption peak at 400 nm wavelength. A good linear fit was obtained for the catalytic reduction of 4-NP with Pd/MFCNC, which is consistent with the theoretical pseudo-first order model. Using the equation below, the apparent kinetic rate constant ( $k_{app}$ ) was obtained from the slope of the line and the value was determined to be  $5.83 \times 10^{-3} \text{ s}^{-1}$ .

$$\ln\left(\frac{C_t}{C_0}\right) = \ln\left(\frac{A_t}{A_0}\right) = -k_{app}t \quad (4)$$

where  $C_0$  and  $C_t$  are the concentration of 4-NP initially and at time  $t$ .

To assess the catalytic efficiency with respect to other supported Pd nanocatalysts, the turnover frequency (TOF, defined as number of moles of 4-NP reduced per mole catalyst per hour) was calculated based on the following equation:

$$\text{TOF} = \frac{n(4 - \text{NP})}{22.64\% \times \frac{m(\text{PdMFCNC})}{\text{Mw}(\text{Pd})}} \times k_{app} \quad (5)$$

where  $n$  is the number of moles,  $k_{app}$  is the apparent kinetic rate constant,  $m$  is the mass of the composite catalyst, 22.64% is the mass fraction of Pd in the hybrid catalyst, and  $\text{Mw}$  is the molecular weight of Pd which is 106.42 g/mol. In a typical test, the amount of 4-NP reduced in 1 mL cuvette is 0.08 mmol, and the total mass of hybrid catalyst used is 0.25  $\mu\text{g}$ .

The high activity of our Pd/MFCNC can be largely attributed to the monodispersed fine-sized Pd NP and the homogeneous deposition achieved with the aid of the MFCNC substrate. The synthesis of Pd NPs on MFCNCs is advantageous in the following ways: (i) CNCs provide a high surface area and stabilizing effect due to their hydrophilicity; (ii) MF resin coating further increases the surface area of CNCs because of its sponge-like structure; (iii) the abundant mesopores of the MF resin enhance the immobilization of MNPs by steric hindrance that controls the particle growth and reduces particle aggregation; (iv) the rich nitrogen functional groups of MF offer additional stabilizing effect due to the chelation of MNPs with MF.

Finally, the recyclability of the Pd/MFCNCs were conducted by scale-up of the catalytic reaction to 300 mL. The setup is illustrated in Figure S2a where Pd/MFCNCs were confined in an ultrafiltration cell by a filtration membrane with 100 nm pore size. The reaction mixture was well mixed with the catalyst under magnetic stirring for 13 min before filtration. The filtrate was rapidly transferred to the cuvette for UV-vis measurements. Then the catalyst was washed several times with DI water before the next reaction was conducted. The adsorption peak at 400 nm was all zero in the 10 cycles we conducted (Figure S2b), showing excellent recoverability of the catalyst.

Table 1 shows TOF values for various hybrid Pd nanocatalysts systems that were characterized in terms of the substrate

**Table 1. Comparison of the Catalytic Performance and Origins of Pd Nanocatalyst Supported on Various Substrates for 4-NP Reduction Reaction**

catalyst support/ template	reducing reagent/ method	palladium size (nm)	TOF (h <sup>-1</sup> )	ref
functionalized carbon nanotubes	H <sub>2</sub>	1.5	1080	46
mesoporous silica SBA15	H <sub>2</sub>	7–8	19.1	47
hollow mesoporous ceria	NaBH <sub>4</sub>	3–5	1068	48
double-shelled reduced graphene and carbon	graphene oxide	4	273.6	49
core-shell polyaniline/SnO <sub>2</sub> nanorods	polyaniline	3	493.2	50
cellulose nanocrystal	hydrothermal	1–40	879.5	24
highly porous MF coated cellulose nanocrystal	ethylene glycol	1.5	3168	this work

material, Pd NP size, and reducing method. Our MFCNC supported Pd NP exhibits superior catalytic performance with a TOF value of 3168 h<sup>-1</sup> which is much higher than those of previous reported studies. Since the catalytic reduction occurs at the surface of the Pd NPs, the efficiency is critically dependent on the surface area of the catalyst.

## CONCLUSION

In this study, a novel strategy for synthesizing supported metal nanocatalysts with highly porous core–shell structured MFCNC as the substrate was proposed. The pivotal coating of MF layer provides a favorable substrate for metal deposition because of a high surface area of 212.8 m<sup>2</sup> g<sup>-1</sup> (pristine CNC: 24.12 m<sup>2</sup> g<sup>-1</sup>), a mesoporous structure with a high pore volume of 0.071 cm<sup>3</sup> g<sup>-1</sup> (pristine CNC: 0.001 cm<sup>3</sup> g<sup>-1</sup>), and rich nitrogen functionality. Pt and Pd NPs of between 1 and 2 nm in size were reduced and immobilized uniformly on the MFCNC substrate. The need for the MF modification to achieve optimal MNP synthesis is confirmed by the extremely poor metal deposition when pristine CNCs were used as the substrate. Our synthesized Pd/MFCNCs possessed outstanding catalytic performance with a TOF value of 3168 h<sup>-1</sup> for the reduction of 4-NP. The superior activity is largely attributed to the small particle size and uniform MNP deposition achieved with porous MFCNCs. Our strategy of using MF resin to modify the physiochemical property of CNCs is believed to be promising for synthesizing various metal nanocatalysts with monodisperse ultrafine particle size and superior catalytic activity.

## ASSOCIATED CONTENT

### Supporting Information

The Supporting Information is available free of charge on the ACS Publications website at DOI: [10.1021/acssuschemeng.6b00551](https://doi.org/10.1021/acssuschemeng.6b00551).

Figures S1 and S2 as described in the text ([PDF](#))

## AUTHOR INFORMATION

### Corresponding Author

\*E-mail: [mkctam@uwaterloo.ca](mailto:mkctam@uwaterloo.ca).

### Notes

The authors declare no competing financial interest.

## ACKNOWLEDGMENTS

We wish to acknowledge FP Innovations and CelluForce Inc. for providing the cellulose nanocrystals. The research funding from CelluForce and AboraNano facilitated the research on conductive CNC. K. C. Tam wishes to acknowledge fundings from CFI and NSERC.

## REFERENCES

- Campelo, J. M.; Luna, D.; Luque, R.; Marinas, J. M.; Romero, A. A. Sustainable preparation of supported metal nanoparticles and their applications in catalysis. *ChemSusChem* **2009**, *2* (1), 18–45.
- Bastakoti, B. P.; Li, Y.; Miyamoto, N.; Sanchez-Ballester, N. M.; Abe, H.; Ye, J.; Srinivasu, P.; Yamauchi, Y. Polymeric micelle assembly for the direct synthesis of functionalized mesoporous silica with fully accessible Pt nanoparticles toward an improved CO oxidation reaction. *Chem. Commun.* **2014**, *50* (65), 9101–9104.
- Shen, D.; Chen, L.; Yang, J.; Zhang, R.; Wei, Y.; Li, X.; Li, W.; Sun, Z.; Zhu, H.; Abdullah, A. M.; et al. Ultradispersed Palladium Nanoparticles in Three-Dimensional Dendritic Mesoporous Silica Nanospheres: Toward Active and Stable Heterogeneous Catalysts. *ACS Appl. Mater. Interfaces* **2015**, *7* (31), 17450–17459.
- Zhao, M.; Deng, K.; He, L.; Liu, Y.; Li, G.; Zhao, H.; Tang, Z. Core–shell palladium nanoparticle@ metal–organic frameworks as multifunctional catalysts for cascade reactions. *J. Am. Chem. Soc.* **2014**, *136* (5), 1738–1741.
- Aijaz, A.; Zhu, Q.-L.; Tsumori, N.; Akita, T.; Xu, Q. Surfactant-free Pd nanoparticles immobilized to a metal–organic framework with size-and location-dependent catalytic selectivity. *Chem. Commun.* **2015**, *51* (13), 2577–2580.
- Chen, Y.; Zhu, Q. L.; Tsumori, N.; Xu, Q. Immobilizing highly catalytically active noble metal nanoparticles on reduced graphene oxide: A non-noble metal sacrificial approach. *J. Am. Chem. Soc.* **2015**, *137* (1), 106–109.
- Epshteyn, A.; Garsany, Y.; More, K. L.; Meyer, H. M., III; Jain, V.; Purdy, A. P.; Swider-Lyons, K. E. Effective Strategy for Improving Electrocatalyst Durability by Adhesive Immobilization of Catalyst Nanoparticles on Graphitic Carbon Supports. *ACS Catal.* **2015**, *5*, 3662–3674.
- Lin, X.; Wu, M.; Wu, D.; Kuga, S.; Endo, T.; Huang, Y. Platinum nanoparticles using wood nanomaterials: eco-friendly synthesis, shape control and catalytic activity for p-nitrophenol reduction. *Green Chem.* **2011**, *13* (2), 283–287.
- Xue, Z.; Sun, X.; Li, Z.; Mu, T. CO<sub>2</sub> as a regulator for the controllable preparation of highly dispersed chitosan-supported Pd catalysts in ionic liquids. *Chem. Commun.* **2015**, *51*, 10811–10814.
- Budarin, V. L.; Clark, J. H.; Luque, R.; Macquarrie, D. J.; White, R. J. Palladium nanoparticles on polysaccharide-derived mesoporous materials and their catalytic performance in C–C coupling reactions. *Green Chem.* **2008**, *10* (4), 382–387.
- Gronnow, M. J.; Luque, R.; Macquarrie, D. J.; Clark, J. H. A novel highly active biomaterial supported palladium catalyst. *Green Chem.* **2005**, *7* (7), 552–557.
- Rajender Reddy, K.; Kumar, N. S.; Surendra Reddy, P.; Sreedhar, B.; Lakshmi Kantam, M. Cellulose supported palladium(0) catalyst for Heck and Sonogashira coupling reactions. *J. Mol. Catal. A: Chem.* **2006**, *252* (1–2), 12–16.
- Lahiji, R. R.; Xu, X.; Reifenberger, R.; Raman, A.; Rudie, A.; Moon, R. J. Atomic Force Microscopy Characterization of Cellulose Nanocrystals. *Langmuir* **2010**, *26* (6), 4480–4488.
- Habibi, Y. Key advances in the chemical modification of nanocelluloses. *Chem. Soc. Rev.* **2014**, *43* (5), 1519–1542.
- Cirtiu, C. M.; Dunlop-Brière, A. F.; Moores, A. Cellulose nanocrystallites as an efficient support for nanoparticles of palladium: application for catalytic hydrogenation and Heck coupling under mild conditions. *Green Chem.* **2011**, *13* (2), 288–291.
- Lam, E.; Hrapovic, S.; Majid, E.; Chong, J. H.; Luong, J. H. T. Catalysis using gold nanoparticles decorated on nanocrystalline cellulose. *Nanoscale* **2012**, *4* (3), 997–1002.

- (17) Koga, H.; Tokunaga, E.; Hidaka, M.; Umemura, Y.; Saito, T.; Isogai, A.; Kitaoka, T. Topochemical synthesis and catalysis of metal nanoparticles exposed on crystalline cellulose nanofibers. *Chem. Commun. (Cambridge, U.K.)* **2010**, *46*, 8567–8569.
- (18) Wu, X.; Lu, C.; Zhou, Z.; Yuan, G.; Xiong, R.; Zhang, X. Green synthesis and formation mechanism of cellulose nanocrystal-supported gold nanoparticles with enhanced catalytic performance. *Environ. Sci.: Nano* **2014**, *1* (1), 71–79.
- (19) Chen, L.; Cao, W.; Quinlan, P. J.; Berry, R. M.; Tam, K. C. Sustainable Catalysts from Gold-Loaded Polyamidoamine Dendrimer-Cellulose Nanocrystals. *ACS Sustainable Chem. Eng.* **2015**, *3* (5), 978–985.
- (20) Tang, J.; Shi, Z.; Berry, R. M.; Tam, K. C. Mussel-inspired green metallization of silver nanoparticles on Cellulose Nanocrystals and their enhanced catalytic reduction of 4-Nitrophenol in the presence of  $\beta$ -cyclodextrin. *Ind. Eng. Chem. Res.* **2015**, *54* (13), 3299–3308.
- (21) Johnson, L.; Thielemans, W.; Walsh, D. A. Synthesis of carbon-supported Pt nanoparticle electrocatalysts using nanocrystalline cellulose as reducing agent. *Green Chem.* **2011**, *13* (7), 1686–1693.
- (22) Benaissi, K.; Johnson, L.; Walsh, D. A.; Thielemans, W. Synthesis of platinum nanoparticles using cellulosic reducing agents. *Green Chem.* **2010**, *12*, 220.
- (23) Rezayat, M.; Blundell, R. K.; Camp, J. E.; Walsh, D. A.; Thielemans, W. Green One-Step Synthesis of Catalytically Active Palladium Nanoparticles Supported on Cellulose Nanocrystals. *ACS Sustainable Chem. Eng.* **2014**, *2* (5), 1241–1250.
- (24) Wu, X.; Lu, C.; Zhang, W.; Yuan, G.; Xiong, R.; Zhang, X. A novel reagentless approach for synthesizing cellulose nanocrystal-supported palladium nanoparticles with enhanced catalytic performance. *J. Mater. Chem. A* **2013**, *1* (30), 8645.
- (25) Shi, Z.; Tang, J.; Chen, L.; Yan, C.; Tanvir, S.; Anderson, W. A.; Berry, R. M.; Tam, K. C. Enhanced colloidal stability and antibacterial performance of silver nanoparticles/cellulose nanocrystal hybrids. *J. Mater. Chem. B* **2015**, *3* (4), 603–611.
- (26) Astruc, D.; Lu, F.; Aranzaes, J. R. Nanoparticles as recyclable catalysts: the frontier between homogeneous and heterogeneous catalysis. *Angew. Chem., Int. Ed.* **2005**, *44* (48), 7852–7872.
- (27) Karimi, B.; Abedi, S.; Clark, J. H.; Budarin, V. Highly Efficient Aerobic Oxidation of Alcohols Using a Recoverable Catalyst: The Role of Mesoporous Channels of SBA-15 in Stabilizing Palladium Nanoparticles. *Angew. Chem.* **2006**, *118* (29), 4894–4897.
- (28) Filik, H.; et al. Separation and preconcentration of iron(II) and iron(III) from natural water on a melamine-formaldehyde resin. *Talanta* **1997**, *44* (5), 877–884.
- (29) Baraka, A.; Hall, P. J.; Heslop, M. J. Preparation and characterization of melamine-formaldehyde-DTPA chelating resin and its use as an adsorbent for heavy metals removal from wastewater. *React. Funct. Polym.* **2007**, *67* (7), 585–600.
- (30) Wu, Y.; Li, Y.; Qin, L.; Yang, F.; Wu, D. Monodispersed or narrow-dispersed melamine-formaldehyde resin polymer colloidal spheres: preparation, size-control, modification, bioconjugation and particle formation mechanism. *J. Mater. Chem. B* **2013**, *1* (2), 204–212.
- (31) Merline, D. J.; Vukusic, S.; Abdala, A. A. Melamine formaldehyde: curing studies and reaction mechanism. *Polym. J.* **2013**, *45* (4), 413–419.
- (32) Kim, K.; Lee, J. Y. Microencapsulation of Electrophoretic TiO<sub>2</sub> Nanoparticles for Electronic Ink Materials Microencapsulation. *Mol. Cryst. Liq. Cryst.* **2006**, *445*, 333–338.
- (33) Geder, J.; Hoster, H. E.; Jossen, A.; Garche, J.; Yu, D. Y. W. Impact of active material surface area on thermal stability of LiCoO<sub>2</sub> cathode. *J. Power Sources* **2014**, *257*, 286–292.
- (34) Fumagalli, M.; Sanchez, F.; Boisseau, S. M.; Heux, L. Gas-phase esterification of cellulose nanocrystal aerogels for colloidal dispersion in apolar solvents. *Soft Matter* **2013**, *9* (47), 11309–11317.
- (35) Han, J.; Zhou, C.; Wu, Y.; Liu, F.; Wu, Q. Self-assembling behavior of cellulose nanoparticles during freeze-drying: Effect of suspension concentration, particle size, crystal structure, and surface charge. *Biomacromolecules* **2013**, *14* (5), 1529–1540.
- (36) Yang, X.; Cranston, E. D. Chemically Cross-Linked Cellulose Nanocrystal Aerogels with Shape Recovery and Superabsorbent Properties. *Chem. Mater.* **2014**, *26* (20), 6016–6025.
- (37) Brunauer, S.; Deming, L. S.; Deming, W. E.; Teller, E. On a theory of the van der Waals adsorption of gases. *J. Am. Chem. Soc.* **1940**, *62* (7), 1723–1732.
- (38) Sing, K. S. W.; Everett, D. H.; Haul, R. A.; Moscou, L.; Pierotti, R. A.; Rouquerol, J.; Siemieniewska, T. Reporting physisorption data for gas/solid systems. *Pure Appl. Chem.* **1985**, *57* (4), 603–619.
- (39) Chen, Z.; Wang, J.; Yu, F.; Zhang, Z.; Gao, X. Preparation and properties of graphene oxide-modified poly(melamine-formaldehyde) microcapsules containing phase change material n-dodecanol for thermal energy storage. *J. Mater. Chem. A* **2015**, *3* (21), 11624–11630.
- (40) Sèbe, G.; Ham-Pichavant, F.; Pecastaings, G. Dispersibility and emulsion-stabilizing effect of cellulose nanowhiskers esterified by vinyl acetate and vinyl cinnamate. *Biomacromolecules* **2013**, *14*, 2937–2944.
- (41) Mu, Y.; Liang, H.; Hu, J.; Jiang, L.; Wan, L. Controllable pt nanoparticle deposition on carbon nanotubes as an anode catalyst for direct methanol fuel cells. *J. Phys. Chem. B* **2005**, *109* (47), 22212–22216.
- (42) Kim, S.-W.; Park, J.; Jang, Y.; Chung, Y.; Hwang, S.; Hyeon, T.; Kim, Y. W. Synthesis of Monodisperse Palladium Nanoparticles. *Nano Lett.* **2003**, *3* (9), 1289–1291.
- (43) Scherrer, P. Bestimmung der Größe und der inneren Struktur von Kolloidteilchen mittels Röntgenstrahlen. *Nachrichten von der Gesellschaft der Wissenschaften zu Göttingen, Math. Klasse* **1918**, *2*, 98–100.
- (44) Hervés, P.; Pérez-Lorenzo, M.; Liz-Marzán, L. M.; Dzubiella, J.; Lu, Y.; Ballauff, M. Catalysis by metallic nanoparticles in aqueous solution: model reactions. *Chem. Soc. Rev.* **2012**, *41*, 5577–5587.
- (45) Isayev, O.; Rasulev, B.; Gorb, L.; Leszczynski, J. Structure-toxicity relationships of nitroaromatic compounds. *Mol. Diversity* **2006**, *10* (2), 233–245.
- (46) Gu, X.; Qi, W.; Xu, X.; Sun, Z.; Zhang, L.; Liu, W.; Pan, X.; Su, D. Covalently functionalized carbon nanotube supported Pd nanoparticles for catalytic reduction of 4-nitrophenol. *Nanoscale* **2014**, *6* (12), 6609–6616.
- (47) Morère, J.; Tenorio, M. J.; Torralvo, M. J.; Pando, C.; Renuncio, J. A. R.; Cabañas, A. Deposition of Pd into mesoporous silica SBA-15 using supercritical carbon dioxide. *J. Supercrit. Fluids* **2011**, *56* (2), 213–222.
- (48) Liu, B.; Yu, S.; Wang, Q.; Hu, W.; Jing, P.; Liu, Y.; Jia, W.; Liu, Y.; Liu, L.; Zhang, J. Hollow mesoporous ceria nanoreactors with enhanced activity and stability for catalytic application. *Chem. Commun. (Cambridge, U.K.)* **2013**, *49* (36), 3757–3759.
- (49) Zhang, Z.; Xiao, F.; Xi, J.; Sun, T.; Xiao, S.; Wang, H.; Wang, S.; Liu, Y. Encapsulating Pd Nanoparticles in Double-Shelled Graphene@Carbon Hollow Spheres for Excellent Chemical Catalytic Property. *Sci. Rep.* **2014**, *4*, 1–5.
- (50) Lu, X.; Xue, Y.; Nie, G.; Wang, C. Ultrahigh active pd nanocatalyst supported on core-sheath conducting polymer/metal oxide composite nanorods. *Catal. Lett.* **2012**, *142* (5), 566–572.